Proceedings of the 50th International School & Conference on the Physics of Semiconductors

Electrical Properties of $Yb_{2-x}V_xO_{3+x}$ Nanomaterials Obtained Mechanochemically from Yb_2O_3 and V_2O_5 Oxides

B. Sawicki[a], M. Piz[b], E. Filipek[b], T. Groń[a,*], P. Urbanowicz[a], H. Duda[a], A.Z. Szeremeta[a] and S. Pawlus[a]

[a] *Institute of Physics, University of Silesia in Katowice, 40-007 Katowice, Poland*
[b] *Faculty of Chemical Technology and Engineering, West Pomeranian University of Technology in Szczecin, 70-310 Szczecin, Poland*

Doi: 10.12693/APhysPolA.142.637 *e-mail: tadeusz.gron@us.edu.pl

Electrical measurements were carried out on nanocrystals $Yb_{2-x}V_xO_{3+x}$ (YbVO) (where $x = 0.10$, 0.15, 0.20, 0.30, and 0.40) obtained in the high-energy ball milling process, which crystallite size increased from 23.3 to 42.4 nm with increasing vanadium content. Electrical conductivity and thermoelectric power studies showed insulating properties in the extrinsic region (77–300 K) and n-type semiconductivity in the intrinsic one (350–400 K) with an activation energy of 1.3 eV. Broadband dielectric spectroscopy studies showed a low relative dielectric permittivity ($\varepsilon_r < 16$) and loss tangent ($\tan(\delta) < 0.05$) weakly dependent on temperature and frequency with the exception of a wide maximum between 200 and 300 K, suggesting an antiferroelectric-paraelectric phase transition. The most interesting result is the observation of a strong increase in the thermoelectric power factor with an increase in unit cell volume and nanograin size in a highly thermally activated Arrhenius region.

topics: nanomaterials, electrical conductivity, thermoelectric power, dielectric spectroscopy

1. Introduction

The interest in the phases of solid solutions containing rare earths stems from a wide range of their potential applications. They are used, among others, as plasma displays, electro-luminescent diodes or fluorescence lamps, photocatalysts, scintillators, thermophosphors, and laser-host crystals [1–5]. The solid solutions formed in the binary system of V_2O_5 and Yb_2O_3 oxides show the structure of vanadium (V) oxide and/or ytterbium (III) oxide. It is known from the literature that V_2O_5 oxide is an n-type paramagnetic insulator [6] that is applied in the production of novel materials used, e.g., in medicine [7] or as electrodes in lithium batteries [8]. Yb_2O_3 oxide has the rare-earth *C*-type sesquioxide cubic structure, which is related to the fluorite structure with one-quarter of the anions removed, leading to ytterbium atoms in two different six-coordinate (non-octahedral) environments [9].

Recently it has been established that in the binary system of V_2O_5–Yb_2O_3 oxides in solid-state and in air atmosphere, a substitutive solid solution is formed with limited solubility of components [10]. It is known that the solid solution was obtained only by high-energy ball milling of mixtures of oxides V_2O_5 with Yb_2O_3, containing vanadium (V) oxide in amounts not exceeding 30 mol%. In this solid solution, V^{5+} ions are incorporated into the crystal lattice of ytterbium oxide, replacing Yb^{3+} ions, which leads to the generation of excessive positive charge. Therefore its general formula can be described either as $Yb_{2-5x}\square_{2x}V_{3x}O_3$, where $0.00 < x < 0.1667$, or as $Yb_{2-x}V_xO_{3+x}$, where $0.00 < x < 0.60$ [10]. The authors have also shown for the same nanomaterials that with increasing x in $Yb_{2-5x}\square_{2x}V_{3x}O_3$ or $Yb_{2-x}V_xO_{3+x}$, the crystal lattice of the solid solution unexpectedly expands [10]. As shown by the results of X-ray diffraction (XRD) and ultraviolet-visible diffraction (UV-Vis-DR) measurements, the nanoparticles of the solid solution of V_2O_5 in Yb_2O_3 crystallize in a cubic system and have an energy gap value of 2.5 eV [10].

In our group, extensive electrical research was carried out on compounds and solid solutions based on vanadium oxide. In Nb_2VSbO_{10} ceramics, the n-type semiconducting and both symmetric and non-linear behavior (back-to-back varistor-like) of the *I*–*V* characteristics were observed [11]. In $Fe_{1-x}Cr_xVSbO_6$ semiconducting solid solution, n-type conductivity was observed for samples richer in Fe, and a change in the Seebeck coefficient (from n to p) — for samples richer in Cr [12]. In the n-type semiconductor ceramics $Nb_6VSb_3O_{25}$, a wide minimum conductance, $G(V)$, was found, which

shifted towards higher voltages, and at the same time, its value decreased with increasing temperature [13]. Additionally, the relaxation process in these ceramic materials was identified, which was strongly obscured by DC conductivity with comparable activation energies [14]. In the $Cu_2In_3VO_9$ ceramics, semiconducting properties, an energy gap of 1.09 eV, a relaxation process, and a strong emission of charge carriers due to temperature and voltage were found [15].

In turn, it was found that the multicomponent system of $M_2FeV_3O_{11}$ oxides (M = Mg, Zn, Pb, Co, Ni) exhibits highly thermally activated semiconducting properties above room temperature, n-type conductivity at higher temperatures, higher conductivity for ceramics containing Co^{2+}, Ni^{2+}, and Mg^{2+} ions and strong dependence of the relative dielectric constant and loss tangent on temperature and frequency [16]. The $Yb_{8-x}Y_xV_2O_{17}$ phases for $x = 0, 2$ and 8 turned out to be insulators with a band gap of 2.6 eV, low electrical conductivity (mainly n-type), with a characteristic minimum shifting towards higher temperatures in the sequence $x = 0, 2$ and 8. Their electrical conductivity decreased with increasing ytterbium content, and the breakdown voltage oscillated around the value of 26 V/mm and was characteristic (or typical) of the varistor behavior [17]. Next, $Zn_{2-x}Mg_xInV_3O_{11}$ materials (where x = 0.0, 0.4, 1.0, 1.6, and 2.0) showed n-type semiconducting properties with activation energies of 0.147–0.52 eV in the temperature range of 250–400 K, symmetrical and linear I–V characteristics at both 300 K and 400 K, stronger carrier emission for the $Zn_2InV_3O_{11}$ matrix and much lower for the remaining samples, and dipole relaxation, which was slower for the sample with $x = 0.0$ (matrix) and faster for the Mg-doped samples with $x > 0.0$ [18, 19].

The main motivation for selecting the $Yb_{2-x}V_xO_{3+x}$ (labeled later as YbVO) ternary phase for electrical research is that Yb^{3+} is a paramagnetic ion with a strongly screened $4f$ subshell. In turn, vanadium ions can be in the 2nd, 3rd, 4th, and 5th valence states, with the latter being the dominant state.

2. Experimental details

2.1. Synthesis of nanocrystals

The following reagents were used to synthesize solid solutions: Yb_2O_3, a.p. (analytically pure) (Alfa Aesar, Germany), and V_2O_5, a.p. (POCh, Poland). The synthesis of five samples for the purpose of this work was carried out by the high-energy mechanical alloying milling method using laboratory planetary ball mill PULVERISETTE 6 (Fritsch GmbH, Germany) with vessel and balls of zirconium, rpm = 500, BPR (ball-to-powder ratio) = 1:20, time = 3 and once again 3 h under air atmosphere. Details referring to the conducted syntheses and the phase composition, as well as some properties of the samples examined using the XRD, infrared spectroscopy (IR), and scanning electron microscopy (SEM) methods were given in [10]. A visualization of the cubic structure of the $Yb_{2-x}V_xO_{3+x}$ solid solution is shown in Fig. 1, and its average size of crystallites (d), lattice parameter (a), unit cell volume (V), and the experimental (d_{exp}) and calculated (d_{rtg}) densities are given in Table I.

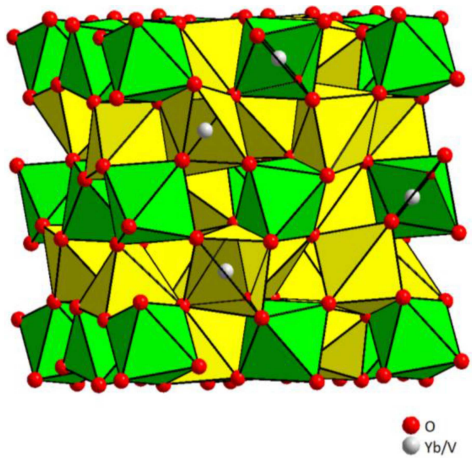

Fig. 1. Visualization of the cubic structure of the YbVO solid solution. White balls represent Yb^{3+}/V^{5+}, red balls — O^{2-}.

TABLE I

Average size of crystallites, d, determined by the Scherrer's method for nanocrystals of YbVO solid solution obtained by the mechanochemical method. Here, x is the vanadium content, a is the lattice parameter, V is the unit cell volume, and d_{exp} and d_{rtg} are the experimental and calculated densities, respectively

x	d [nm]	a [nm]	V [nm^3]	d_{exp} [g/cm^3]	d_{rtg} [g/cm^3]
0.10	23.3	1.0426	1.1333	8.66	8.99
0.15	26.9	1.0427	1.1336	8.51	8.86
0.20	31.6	1.0429	1.1343	8.31	8.73
0.30	40.5	1.0436	1.1366	7.92	8.47
0.40	42.4	1.0446	1.1399	7.66	8.20

2.2. Methods

The powder diffraction patterns of the samples obtained were recorded on a diffractometer EMPYREAN II (PANalytical, Eindhoven, Netherlands) using Cu K_α with graphite monochromator. The densities of the powdered samples (d_{exp}) were determined using a gas pycnometer (Ultrapyc 1200e, Quantachrome Instruments, Boynton Beach, FL, USA), and argon with a 5N purity was used as the pycnometric gas.

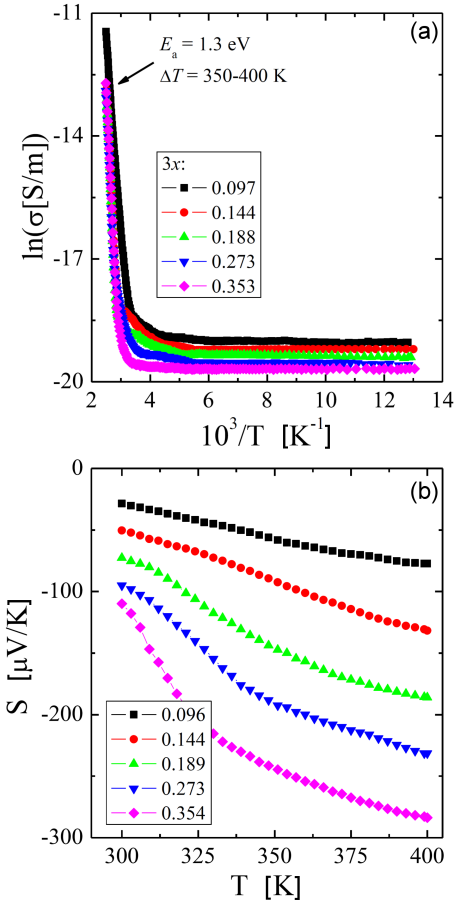

Fig. 2. (a) Electrical conductivity ($\ln\sigma$) vs reciprocal temperature, where E_a is the activation energy. (b) Thermoelectric power S vs temperature T of $Yb_{2-x}V_xO_{3+x}$ nanocrystals.

Electrical conductivity $\sigma(T)$ of the samples under study was measured by the DC method using a KEITHLEY 6517B Electrometer/High Resistance Meter (Keithley Instruments, LLC, Solon, OH, USA) and within the temperature range of 77–400 K. The thermoelectric power $S(T)$, i.e., the Seebeck coefficient, was measured within the temperature range of 300–400 K with the help of a Seebeck Effect Measurement System (MMR Technologies, Inc., San Jose, CA, USA). Dielectric measurements were carried out on pellets of YbVO materials, which were polished as well as sputtered with ($\sim$ 80 nm) Ag electrodes. The studies were carried out in the frequency range from 5×10^2 to 10^6 Hz using an LCR HiTESTER (HIOKI 3532–50, Nagano, Japan) and within the temperature range of 80–400 K. For the electrical and dielectric measurements, the powder samples were compacted in a disc form (10 mm in diameter and 1–2 mm thick) using the pressure of 1.5 GPa; then, they were sintered for 2 h at 923 K. The electrical and thermal contacts were made using a silver lacquer mixture (Degussa Leitsilber 2000, Degussa Gold und Silber, Munich, Germany).

3. Results and discussion

3.1. Grain size and density estimation

The grain size of the YbVO solid solution was determined by Scherrer's method. The analysis of the crystallite sizes showed that they change with the degree of incorporation of V^{5+} ions in place of Yb^{3+} ions into the structure of Yb_2O_3. As the degree of incorporation of vanadium (V) ions increases, the crystallite size of the obtained solid solution increases from $\sim$ 9.0 (for $x = 0$) to $\sim$ 42.4 nm (for $x = 0.4$) (Table I). The crystallites of the YbVO solid solution had a morphology similar to that of the Yb_2O_3 matrix [9]. They look like deformed polyhedrons of irregular shapes and sizes varying from $\sim$ 25 to $\sim$ 45 nm and were almost identical to those obtained in the paper [10]. The solid-state density values obtained experimentally (d_{exp}) and calculated on the basis of XRD data (d_{rtg}) decreased almost linearly as a function of the vanadium content x (Table I).

3.2. Electrical properties

The results of the electrical measurements of the nanoparticles of $Yb_{2-x}V_xO_{3+x}$ solid solution (where $x = 0.1$, 0.15, 0.2, 0.3, and 0.4) clearly showed two areas of the temperature dependence of electrical conductivity, $\sigma(10^3/T)$: extrinsic in the wide temperature range of 77–300 K, where no thermal activation is observed, and intrinsic in the temperature range of 350–400 K with the strong activation energy of $E_a = 1.3$ eV (Fig. 2a). Despite strong activation in the intrinsic area, the electric conductivity value at 400 K is only 3×10^{-6} S/m. We have low n-type electrical conductivity in the intrinsic area (Fig. 2b). This behavior correlates well with the values of the energy gap of 2.5 eV, which do not depend on the vanadium content in the sample [10].

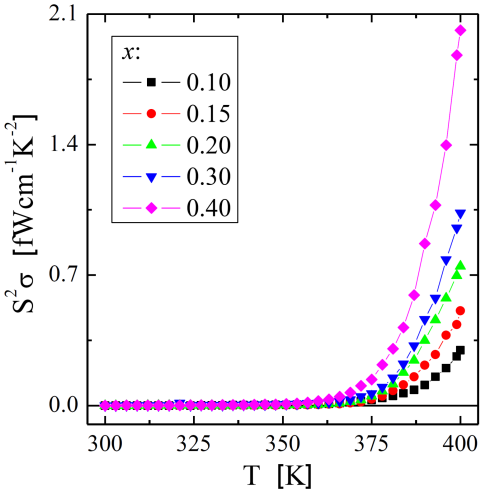

Fig. 3. Power factor $S^2\sigma$ vs temperature T of $Yb_{2-x}V_xO_{3+x}$ nanocrystals.

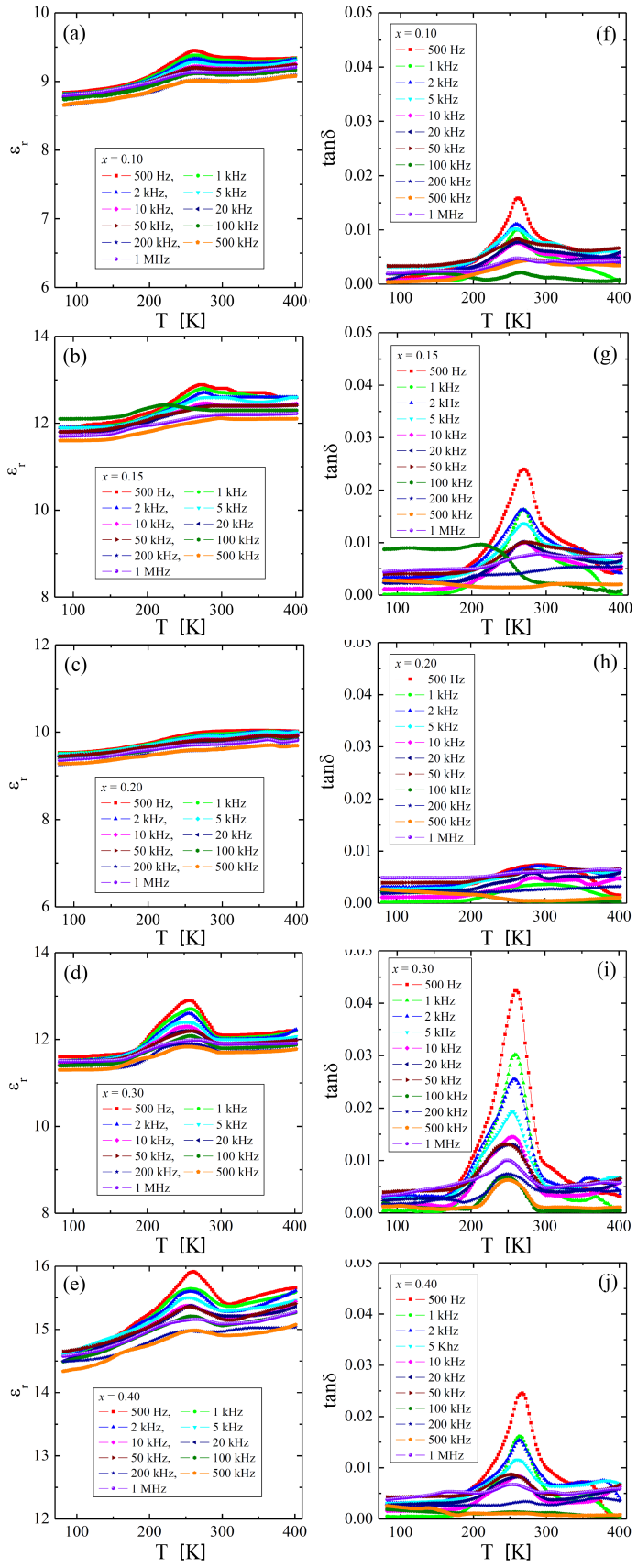

Fig. 4. Relative dielectric permittivity ε_r (a–e) and loss tangent tan(δ) (f–j) vs temperature T of $Yb_{2-x}V_xO_{3+x}$ for $x = 0.10$ (a, f), 0.15 (b, g), 0.20 (c, h), 0.30 (d, i), and 0.40 (e, j) recorded in the frequency range from 500 Hz to 1 MHz.

For comparison, in the cubic $ZnCr_2Se_4$ semiconductor single crystals, in which there are no grain boundaries, the activation energy in the intrinsic region is 10 times lower, i.e., $E_a = 0.135$ eV [20]. The value of E_a increases slightly when the $ZnCr_2Se_4$ matrix is doped with, for example, gallium [20], tin [21], or tantalum [22] ions. Two distinct areas of electrical conductivity with strong activation in the intrinsic region were also observed in ceramics, among others, $Cu_2In_3VO_9$ [15], $M_2FeV_3O_{11}$ (where M = Mg, Zn, Pb, Co, Ni) [16], and $Cd_{1-3x}Gd_{2x}\square_xMoO_4$ [23]. The residual n-type electrical conductivity in the extrinsic region appears to be related to the anion surplus seen in the chemical formula.

Strong activation of electric current carriers in the intrinsic region has a strong influence on the thermoelectric power factor $S^2\sigma$ (Fig. 3), especially for samples with high vanadium content and larger nanograin sizes. It turns out that this is a necessary condition, but not a sufficient one, as all samples have comparable activation energy in the intrinsic region. Therefore, the size effect, in this case, has a decisive influence on the increase of the power factor, since the volume of the unit cell (V) increases with the increase of the vanadium content (x) in the sample (Table I) despite the fact that the vanadium ion (V^{5+}) substituted for ytterbium one (Yb^{3+}) has a smaller ion radius [24]. A similar size effect on the thermoelectric power factor was observed in the case of cobalt and gadolinium-doped calcium molybdato-tungstates [25]. It is well known that the materials with a large power factor value have the most promising thermoelectric properties, especially if they are heavily doped semiconductors, such as Bi_2Te_3 [26].

3.3. Dielectric properties

Figure 4a–e presents the temperature dependence of the relative dielectric permittivity (ε_r) for various electric field frequencies and all studied samples in the content range of $0.1 \leq x \leq 0.4$. As can be seen, for each sample, ε_r undergoes only small changes with increasing frequency and shows a wide maximum in the temperature range of 200–300 K. In addition, the temperature increase is very delicate, e.g., it changes from $\varepsilon_r = 9$ for $x = 0.1$ (Fig. 4a) to $\varepsilon_r = 15$ for $x = 0.4$ (Fig. 4e). The temperature and frequency dependence of $\tan(\delta)$ (Fig. 4f–j) for all samples remains small, below 0.05, and shows a similar maximum as ε_r and greater energy loss than below 200 K and above 300 K, where this loss is below 0.01. Similar behavior with a wide maximum in the $\varepsilon_r(T)$ and $\tan(\delta)(T)$ curves was found in $Ca_{1-x}Mn_xMoO_4$ ($0 \leq x \leq 0.15$) nanomaterials [27]. For comparison, microcrystalline $M_2FeV_3O_{11}$ (M = Mg, Zn, Pb, Co, and Ni) [16] and $MPr_2W_2O_{10}$ (M = Co, Mn) [28] compounds containing $3d$ elements with the unpaired electrons as well as the semiconducting $Zn_{2-x}Mg_xInV_3O_{11}$ ($0 \leq x \leq 2.0$) micromaterials [18, 19] showed both

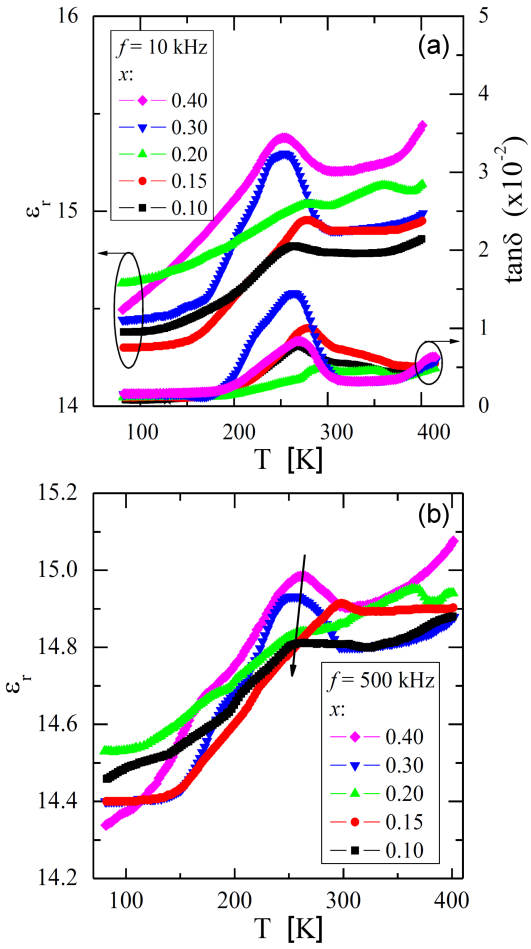

Fig. 5. (a) Temperature dependence of relative dielectric permittivity, $\varepsilon_r(T)$, and loss, $\tan(\delta)(T)$, of $Yb_{2-x}V_xO_{3+x}$ nanocrystals for 10 kHz. (b) Relative dielectric permittivity ε_r vs temperature T of $Yb_{2-x}V_xO_{3+x}$ nanocrystals for 500 kHz. Arrows indicate the evolution of the temperature of a maximum of anomaly.

much higher ε_r and $\tan(\delta)$ than the nanomaterials under study and the $Ca_{1-x}Mn_xMoO_4$ [27] ones mentioned above. This may mean that a small grain size hampers an electric charge accumulation in each sample. This behavior may be the partial recombination of charge carriers in the deep trapping centers [29] lying under the bottom of the conduction band. The natural source of these traps can be grain boundaries with depletion layers of adjacent grains, as it has been observed for ZnO varistors [30, 31], Nb_2VSbO_{10} [11] and $Nb_6VSb_3O_{25}$ [13] ceramics, as well as some novel copper/cobalt and rare-earth metal tungstates [32].

3.4. Dielectric analysis

As mentioned, the temperature dependencies of ε_r and $\tan(\delta)$ show a wide maximum in the 200–300 K temperature range, which decreases with increasing frequency (Fig. 4). At first glance,

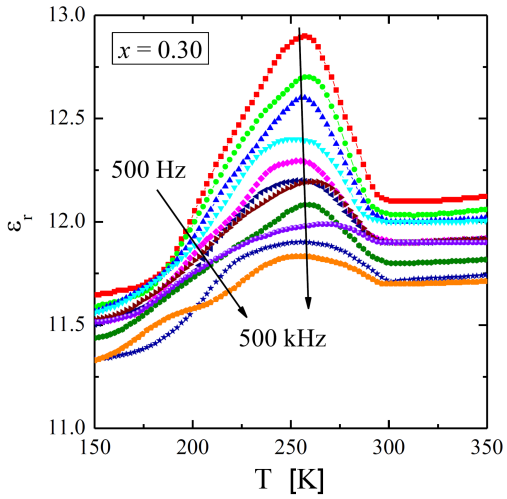

Fig. 6. Temperature dependence of relative dielectric permittivity, $\varepsilon_r(T)$, of $Yb_{2-x}V_xO_{3+x}$ nanocrystals for $x = 0.30$ and various frequencies. Arrow indicate evolution of maximum of anomaly with varying frequency.

this is an obvious anomaly for all samples. To investigate this anomaly, the comparison of ε_r and $\tan(\delta)$ temperature dependence of the YbVO nanoparticles at 10 kHz is shown in Fig. 5a. The value of $\tan(\delta)$ increases rapidly around $T = 250$ K with decreasing temperature. Below $T = 200$ K, the $\tan(\delta)$ value is almost constant.

The spectra for the higher frequencies of 500 kHz are shown in Fig. 5b to compare the evolution of the anomalies respectively for the different samples that are characteristic of the electrical phase transition marked with the arrow. It is clearly seen in Fig. 5a and b that changes in the intensity and temperature of the anomaly are diffuse and not monotonous. For the data measured at a frequency of 500 kHz, it should be noticed that between ca. 120–200 K for all nanomaterials are observed traces of an additional, low-temperature anomaly that may be a trace of a phase transition occurring in the case of one of the components of the mixture. Additionally, the anomaly is also visible above 350 K for $x = 0.2$, which can characterize this particular concentration.

Close inspection of the position of the maximum of the anomaly of $\varepsilon_r(T)$, presented in the case of $x = 0.3$ in Fig. 6, exhibits a subtle evolution of this position with changing frequency. It is worth pointing out that such diffused anomalies reflected the influence of the structural disorder on the phase transitions. According to [33] and [34], this behavior can indicate antiferroelectric-paraelectric (AFE–PE) or antiferroelectric-(ferroelectric)-paraelectric (AFE–FE–PE) phase transitions. The above dielectric analysis shows that in the studied nanoparticles, the polarization of the space charge is dominant, and the electric dipoles are strongly localized. As a result, below the phase transition (i.e., the maximum), the values of ε_r and $\tan(\delta)$ are smaller than above, which may suggest an AFE–PE phase transition rather than FE–PE one.

4. Conclusions

The YbVO nanocrystals obtained in the high-energy ball milling process were characterized by DC electrical conductivity, thermoelectric power, power factor, and dielectric spectroscopy measurements. They have shown insulating properties in the extrinsic region (77–300 K) and n-type semiconductivity in the intrinsic one (350–400 K) with an activation energy of 1.3 eV. Measurements of broadband dielectric spectroscopy and their analysis showed low relative dielectric permittivity ($\varepsilon_r < 16$) and the loss tangent ($\tan(\delta) < 0.05$) weakly dependent on temperature and frequency, except for a wide maximum between 200 and 300 K, suggesting an antiferroelectric-paraelectric phase transition. These studies' most interesting and exciting result is the observation of a strong increase in the thermoelectric power factor $S^2\sigma$ in the highly thermally activated Arrhenius region. This may be mainly due to the size effect, as well as an increase in nanograin size. These studies can be a clue to obtaining a more significant thermoelectric power factor in classic semiconductors or conductors.

References

[1] R.B. Pode, A.M. Band, H.D. Juneja, S.J. Dhoble, *Phys. Status Solidi (a)* **157**, 493 (1996).

[2] J. Chen, F. Guo, N. Zhuang, J. Lan, X. Hu, S. Gao, *J. Cryst. Growth* **243**, 450 (2002).

[3] V. Buissette, A. Huignard, T. Gacoin, J.P. Boilot, P. Aschehoug, B. Viana, *Surf. Sci.* **532**, 444 (2003).

[4] H.Y. Xu, H.Wang, T.N. Jin, H. Yan, *Nanotechnology* **16**, 65 (2005).

[5] Z. Xia, D. Chen, M. Yang, T. Ying, *J. Phys. Chem. Solids* **71**, 175 (2010).

[6] J.B. Goodenough, in: *Progress in Solid State Chemistry*, Vol. 5, Ed. H. Reiss, Pergamon Press, Oxford 1971.

[7] E.V. Arkhipova, M.G. Zuev, L.A. Perelyaeva, *J. Alloys Compd.* **414**, 48 (2006).

[8] N. Kumagai, I. Ikenoya, I. Ishiyama, K. Tanno, *Solid State Ionics* **28–30**, 862 (1988).

[9] A.F. Wells, *Structural Inorganic Chemistry*, Clarendon Press, Oxford 1975, p. 450.

[10] M. Piz, P. Dulian, E. Filipek, K. Wieczorek-Ciurowa, P. Kochmanski, *J. Mater. Sci.* **53**, 13491 (2018).

[11] T. Groń, E. Filipek, M. Piz, H. Duda, T. Mydlarz, *Mater. Res. Bull.* **48**, 2712 (2013).

[12] H. Duda, E. Filipek, G. Dąbrowska, T. Groń, T. Mydlarz, *Acta Phys. Pol. A* **124**, 833 (2013).

[13] T. Groń, E. Filipek, M. Piz, H. Duda, *Mater. Res. Bull.* **51**, 105 (2014).

[14] T. Groń, E. Filipek, M. Piz, Z. Kukuła, S. Pawlus, *Acta Phys. Pol. A* **129**, 355 (2016).

[15] T. Groń, M. Bosacka, E. Filipek, A. Pacześna, P. Urbanowicz, B. Sawicki, H. Duda, *Ceram. Int.* **43**, 2456 (2017).

[16] T. Groń, A. Blonska-Tabero, E. Filipek, P. Urbanowicz, B. Sawicki, H. Duda, Z. Stokłosa, *Ceram. Int.* **43**, 6758 (2017).

[17] B. Sawicki, M. Piz, E. Filipek, T. Groń, H. Duda, *Acta Phys. Pol. A* **132**, 363 (2017).

[18] B. Sawicki, M. Bosacka, E. Filipek, T. Groń, H. Duda, M. Oboz, P. Urbanowicz, *Acta Phys. Pol. A* **134**, 958 (2018).

[19] T. Groń, M. Bosacka, E. Filipek, S. Pawlus, A. Nowok, B. Sawicki, H. Duda, J. Goraus, *Materials* **13**, 2425 (2020).

[20] I. Okońska-Kozłowska, H.D. Lutz, T. Groń, J. Krok, T. Mydlarz, *Mater. Res. Bull.* **19**, 1 (1984).

[21] I. Jendrzejewska, T. Groń, J. Kusz, M. Żelechower, E. Maciążek, A. Ślebarski, M. Fijałkowski, *J. Alloys Compd.* **635**, 238 (2015).

[22] I. Jendrzejewska, T. Groń, P. Kwapuliński, J. Kusz, E. Pietrasik, T. Goryczka, B. Sawicki, A. Ślebarski, M. Fijałkowski, J. Jampilek, H. Duda, *Materials* **14**, 2749 (2021).

[23] B. Sawicki, T. Groń, E. Tomaszewicz, H. Duda, K. Górny, *Ceram. Int.* **41**, 13080 (2015).

[24] R.D. Shannon, *Acta Crystallogr. A* **32**, 751 (1976).

[25] B. Sawicki, M. Karolewicz, E. Tomaszewicz, M. Oboz, T. Groń, Z. Kukuła, S. Pawlus, A. Nowok, H. Duda, *Materials* **14**, 3692 (2021).

[26] G.J. Snyder, T. Caillat, J.P. Fleurial, *Mater. Res. Innovations* **5**, 67 (2001).

[27] T. Groń, M. Karolewicz, E. Tomaszewicz, M. Guzik, M. Oboz, B. Sawicki, H. Duda, Z. Kukuła, *J. Nanopart. Res.* **21**, 8 (2019).

[28] Z. Kukuła, E. Tomaszewicz, S. Mazur, T. Groń, H. Duda, S. Pawlus, S.M. Kaczmarek, H. Fuks, T. Mydlarz, *Philos. Mag.* **92**, 4167 (2012).

[29] C. Li, J. Wang, W. Su, H. Chen, W. Wang, D. Zhuang, *Physica B* **307**, 1 (2001).

[30] L.M. Levinson, H.R. Philipp, *J. Appl. Phys.* **46**, 1332 (1975).

[31] G.D. Mahan, *J. Appl. Phys.* **54**, 3825 (1983).

[32] T. Groń, E. Tomaszewicz, Z. Kukuła, S. Pawlus, B. Sawicki, *Mater. Sci. Eng. B* **184**, 14 (2014).

[33] W-K. Choo, H.-J. Kim, *J . Phys. Condens. Matter* **4**, 2309 (1992).

[34] N. Yasuda, J. Konda, *Appl. Phys. Lett.* **62**, 535 (1993).